

ReflexSplit: Single Image Reflection Separation via Layer Fusion-Separation

Chia-Ming Lee^{1,2} Yu-Fan Lin² Jin-Hui Jiang¹ Yu-Jou Hsiao²
Chih-Chung Hsu^{1,2} Yu-Lun Liu¹

¹National Yang Ming Chiao Tung University ²National Cheng Kung University

Abstract

Single Image Reflection Separation (SIRS) disentangles mixed images into transmission and reflection layers. Existing methods suffer from transmission-reflection confusion under nonlinear mixing, particularly in deep decoder layers, due to implicit fusion mechanisms and inadequate multi-scale coordination. We propose ReflexSplit, a dual-stream framework with three key innovations. (1) Cross-scale Gated Fusion (CrGF) adaptively aggregates semantic priors, texture details, and decoder context across hierarchical depths, stabilizing gradient flow and maintaining feature consistency. (2) Layer Fusion-Separation Blocks (LFSB) alternate between fusion for shared structure extraction and differential separation for layer-specific disentanglement. Inspired by Differential Transformer, we extend attention cancellation to dual-stream separation via cross-stream subtraction. (3) Curriculum training progressively strengthens differential separation through depth-dependent initialization and epoch-wise warmup. Extensive experiments on synthetic and real-world benchmarks demonstrate state-of-the-art performance with superior perceptual quality and robust generalization. Our code is available at <https://github.com/wuw2135/ReflexSplit>.

1. Introduction

Reflection artifacts from transparent media degrade image quality, affecting applications like autonomous driving [35] and industrial inspection [29]. Single Image Reflection Separation (SIRS) disentangles \mathbf{I} into transmission \mathbf{T} and reflection \mathbf{R} layers. Unlike reflection removal treating reflection as noise, SIRS must recover both layers with distinct characteristics, requiring effective disentanglement to prevent inter-layer confusion [42]. Early work modeled this as $\mathbf{I} = \mathbf{T} + \mathbf{R}$ [5], but this ignores layer asymmetry and complementarity, limiting real-world handling.

Subsequent work introduced weighted linear models $\mathbf{I} = \alpha\mathbf{T} + \beta\mathbf{R}$ [32], partially capturing layer asymmetry but relying on fixed global weights. More recently, Hu *et al.* [13] proposed the nonlinear residual formulation

$$\mathbf{I} = \mathbf{T} + \mathbf{R} + \Phi(\mathbf{T}, \mathbf{R}), \quad (1)$$



Figure 1. **Challenging examples on OpenRR-1K [40].** Both DSIT [14] and RDNet [43] exhibit *transmission-reflection confusion* with incomplete reflection separation, leading to annoying artifacts or details distortion. ReflexSplit achieves better separation through explicit fusion-separation and multi-scale coordination.

where $\Phi(\cdot)$ is a learnable nonlinear function modeling intricate inter-layer interactions. To better handle these nonlinear effects and achieve more effective separation of transmission and reflection layers, various methods have been proposed. YTMT [12] and DSRNet [13] enhance inter-layer interaction through activation functions and channel splitting. DSIT [14] strengthens intra-layer feature interaction via dual-stream attention mechanisms. RDNet [43], inspired by the hypercolumn network [9], designs a reversible decoupling network [8] to integrate and propagate multi-scale features, ensuring stable gradient propagation within the entire network—though at the cost of computational complexity and a two-stage training difficulty.

Despite these advances, we observe a persistent phenomenon: when encountering strong reflections (e.g., intense light source reflections in water pools as shown in Fig-

ure 1(a)) or ambiguous scenarios (e.g., a moon painting on a wall being misidentified as reflection in Figure 1(b)), networks incorrectly confuse transmission and reflection layers (*transmission-reflection confusion*), leading to suboptimal performance. Moreover, as commonly observed, increasing network depth often accompanies information loss, causing intra- and inter-layer features to become inseparable [10, 43]. This not only weakens the ability to model nonlinear effects but also exacerbates transmission-reflection confusion, particularly in deep decoder layers (Figure 2).

To address these fundamental challenges, we propose **ReflexSplit**, a dual-stream framework with three key innovations: (1) **Cross-scale Gated Fusion (CrGF)**: Unlike MuGI [13] which exchanges features at individual scales, CrGF adaptively aggregates semantic priors (GFEB), texture details (LFEB), and decoder context across hierarchical depths, stabilizing gradient flow and preventing feature degradation that causes transmission-reflection confusion. (2) **Layer Fusion-Separation Block (LFSB)**: LFSB alternates between fusion and separation. *Early fusion* shares complementary information via bidirectional projection, while *Differential Dual-Dimensional Attention* performs cross-stream subtraction $\mathbf{A}^t - \lambda \mathbf{A}^r$ to suppress interference across spatial and inter-layer dimensions, ensuring layer-specific disentanglement. (3) **Curriculum Training**: Differential separation is progressively strengthened through depth-dependent initialization and epoch-wise warmup, enabling the network to learn holistic reconstruction before focusing on layer-specific separation. As shown in Figure 1, ReflexSplit achieves superior separation under challenging nonlinear mixing where competing methods suffer from severe confusion. Our contributions are:

- **Explicit layer fusion-separation framework**: A paradigm that alternates between fusion for shared degradation extraction and differential separation for layer-specific disentanglement, preventing transmission-reflection confusion throughout the network hierarchy.
- **Cross-scale gated fusion and differential attention**: CrGF adaptively aggregates multi-scale features to maintain hierarchical consistency, while LFSB performs cross-stream attention subtraction for explicit layer disentanglement, stabilized by curriculum training.
- **State-of-the-art performance**: Superior results on both synthetic and real-world benchmarks, demonstrating robust layer separation and strong generalization capability.

2. Related Work

Physical Models for Reflection Superposition. Early reflection removal studies [5, 20, 22] relied on the linear superposition model $\mathbf{I} = \mathbf{T} + \mathbf{R}$, which assumes simple additive mixing between transmission and reflection layers. To capture asymmetric contributions, weighted models such as $\mathbf{I} = \alpha \mathbf{T} + \beta \mathbf{R}$ [32] and $\mathbf{I} = \alpha \mathbf{T} + (1 - \alpha) \mathbf{R}$ [39] introduced

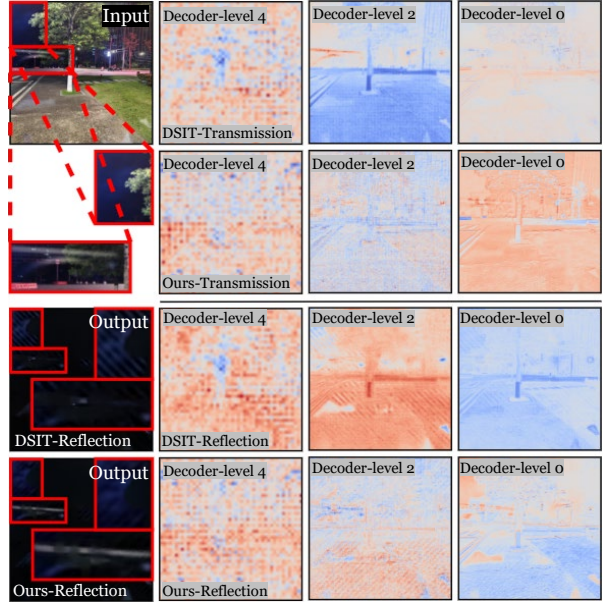


Figure 2. **Layer-wise feature disentanglement comparison.** DSIT [14] suffers from progressive transmission-reflection confusion in deep layers, exhibiting blurred boundaries and residual transmission leakage. Our method maintains clear layer distinction across all depths, preventing feature entanglement and achieving consistent reflection suppression.

global attenuation coefficients α, β . However, these global weights fail to model spatial non-uniformity.

To address this limitation, spatially-varying models emerged. Dong et al. [3] and Wen et al. [37] employed pixel-wise mixing weights \mathbf{W} , e.g., $\mathbf{I} = \mathbf{W} \circ \mathbf{T} + (1 - \mathbf{W}) \circ \mathbf{R}$, enabling adaptive blending across spatial locations. Beyond linear frameworks, Zheng et al. [44] modeled absorption and refraction via spatially-varying coefficients, while Wan et al. [34] introduced nonlinear mappings $\mathbf{I} = g(\mathbf{T}_s) + f(\mathbf{R}_s)$ to learn distinct degradation processes per layer. Most recently, DSRNet [13] proposed the residual formulation $\mathbf{I} = \hat{\mathbf{T}} + \hat{\mathbf{R}} + \varphi(\mathbf{T}, \mathbf{R})$, where a learnable residual term $\varphi(\mathbf{T}, \mathbf{R})$ captures complex nonlinear inter-layer interactions.

Reflection Separation. Early multi-image methods exploited auxiliary cues—polarization [16, 19, 26], focus [6], stereo [28], flash [1, 18], or motion [24, 38]—to reduce ill-posedness, but required specialized equipment or controlled capture, limiting practical deployment. This motivated *Single Image Reflection Separation (SIRS)*, which must disentangle layers from a single observation without auxiliary cues, making explicit inter-layer modeling critical.

Early SIRS works [7, 23, 33] employed multi-stage refinement with implicit complementarity, leading to suboptimal feature exchange. Recent methods formalized explicit interaction: YTMT [12] exchanged suppressed features via ReLU operations; DSRNet [13] introduced Mu-

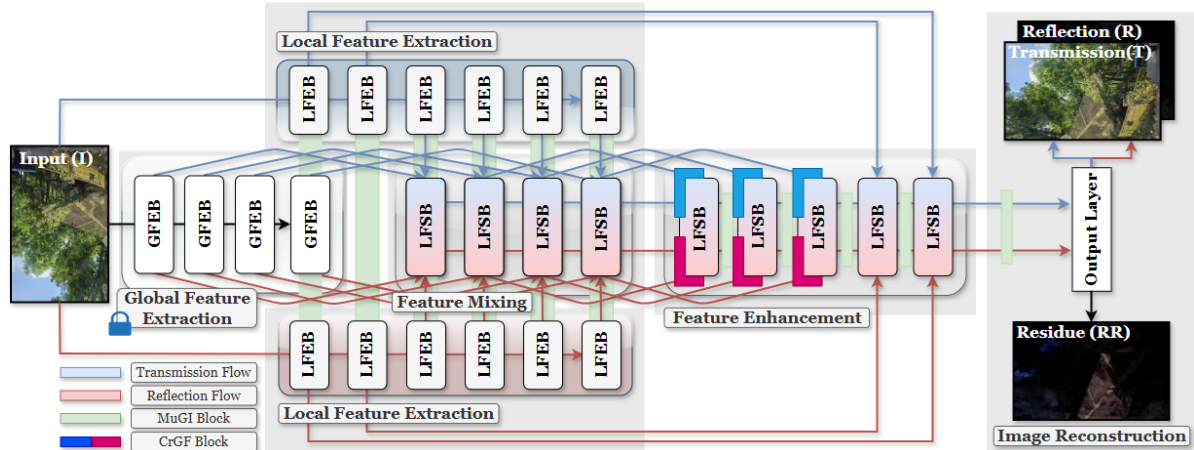


Figure 3. **Overview of ReflexSplit.** Dual-branch encoders extract hierarchical features: GFEB (Swin Transformer) for global semantics $\{P_\ell\}$ and LFEB (MuGI-based) for local textures $\{E_\ell\}$. CrGF (Section 3.1) adaptively aggregates these multi-scale features across decoder depths, while LFSB (Section 3.2) alternates between fusion (cross-stream complementarity) and differential separation (layer disentanglement) to progressively refine dual streams. Curriculum training (Section 3.3) progressively strengthens separation via depth-dependent initialization and epoch-wise warmup. Outputs: T , R , and residual RR , which captures nonlinear interactions.

tual Gated Interaction (MuGI) for dynamic cross-stream control; DSIT [14] combined self- and cross-attention but directly aggregates outputs without separation constraints, causing progressive confusion in deep layers (Figure 2). RDNet [43] uses reversible encoders for lossless flow but lacks explicit scale balancing, while DExNet [15] achieves efficiency through sparse updates at the cost of expressiveness. RobustSIRR [30] enhances robustness via multi-scale attention and feature fusion with adversarial training, but it does not address hierarchical feature entanglement. Complementary approaches explored physical priors—HGRR [46] (hue maps), IBCLN [21] (residual maps), Lei et al. [19] (polarization), PromptRR [45] (multimodal guidance)—yet assume linear mixing and uniform attenuation, failing under over-exposure and specular highlights. DAI [11] deliverer strong results using diffusion priors but at a prohibitive computational cost.

Despite progress, existing methods face two key challenges: inadequate hierarchical feature aggregation causing gradient instability, and implicit fusion mechanisms leading to progressive layer confusion. Our ReflexSplit tackles these through CrGF—which adaptively aggregates multi-scale features—and LFSB—which explicitly enforces layer disentanglement via differential attention.

3. Methodology

Given a mixed image $I \in \mathbb{R}^{H \times W \times 3}$, ReflexSplit decomposes it into transmission T and reflection R layers through explicit layer fusion-separation. As illustrated in Figure 3, our dual-stream architecture comprises three core components: (1) Dual-branch feature extraction combining global semantic priors and local texture details to capture

complementary multi-scale representations; (2) Cross-scale Gated Fusion (CrGF) that adaptively aggregates hierarchical features across decoder depths while stabilizing gradient flow; (3) Layer Fusion-Separation Blocks (LFSB) that alternate between adaptive fusion for shared structure extraction and differential separation for layer-specific disentanglement, preventing transmission-reflection confusion throughout the decoding hierarchy.

Dual-branch Feature Extraction. Following DSIT [14], we separate global semantic modeling from local detail preservation through dual-branch extraction. A pre-trained Swin Transformer [25] serves as the Global Feature Extractor Block (GFEB), extracting semantic priors $\{P_2, P_3, P_4, P_5\}$ at multiple scales. Complementarily, a MuGI-based [13] CNN serves as the Local Feature Extractor Block (LFEB), capturing texture details $\{E_0, E_1, E_2, E_3, E_4, E_5\}$ at hierarchical resolutions $H_\ell = H/2^\ell$, $W_\ell = W/2^\ell$. This dual-branch design mitigates feature entanglement inherent in single-stream encoders, establishing complementary representations for subsequent fusion and separation.

3.1. Cross-scale Gated Fusion

Stable global feature flow is critical for preventing progressive feature degradation and transmission-reflection confusion. While intra-layer mechanisms like MuGI [13] enhance complementarity at individual scales, adaptive cross-scale coordination from heterogeneous sources (semantic priors, texture details, decoder context) is equally essential. Existing methods fall short: DSIT [14] suffers gradient instability; RobustSIRR [30] performs multi-scale fusion via direct concatenation without adaptive gating; RD-

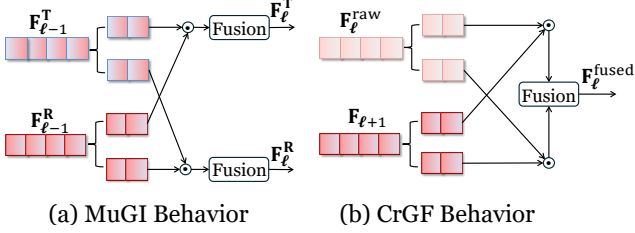


Figure 4. **Complementary roles of MuGI and proposed CrGF.** (a) MuGI [13] focuses on dual-stream *feature interaction*: transmission and reflection features exchange information via channel-wise gating at each decoder level. (b) CrGF focuses on multi-scale *feature integration*: adaptively aggregating hierarchical encoder features and decoder context across scales to maintain gradient stability and feature consistency throughout decoding.

Net [43] lacks explicit scale coordination; MuGI operates only at single scales. Without adaptive cross-scale coordination, these methods struggle to balance semantic richness and fine-grained details across hierarchical depths, leading to progressive feature degradation.

To enable flexible recombination of multi-scale, multi-source features, we propose CrGF at decoder Levels $\{4, 3, 2\}$. As illustrated in Figure 4, CrGF extends MuGI’s gating principle to cross-scale aggregation via bidirectional paths that adaptively balance decoder context ($\mathbf{F}_{\ell+1}$), semantic priors (\mathbf{P}_ℓ), and texture details (\mathbf{E}_ℓ):

$$\begin{cases} \mathbf{F}_\ell^{\text{main}} = \mathcal{G}_1(\mathbf{F}_\ell^{\text{raw}}) \odot \mathcal{G}_2(\mathbf{F}_{\ell+1}); \\ \mathbf{F}_\ell^{\text{aux}} = \mathcal{G}_1(\mathbf{F}_{\ell+1}) \odot \mathcal{G}_2(\mathbf{F}_\ell^{\text{raw}}), \end{cases} \quad (2)$$

where $\mathbf{F}_\ell^{\text{raw}} = \mathbf{F}_{\ell+1} + \mathbf{P}_\ell + \mathbf{E}_\ell$, and $\mathcal{G}_{1,2}$ select complementary channels via splitting. $\mathbf{F}_\ell^{\text{main}}$ emphasizes current-level features gated by context, while $\mathbf{F}_\ell^{\text{aux}}$ propagates context gated by current cues, enabling bidirectional information flow. Final fusion:

$$\mathbf{F}_\ell^{\text{fused}} = w_\ell^{(1)} \phi_1(\mathbf{F}_\ell^{\text{main}}) + w_\ell^{(2)} \phi_2(\mathbf{F}_\ell^{\text{aux}}), \quad (3)$$

where $\phi_{1,2}$ are 1×1 convolutions and w_ℓ normalized by softmax. CrGF’s adaptive bidirectional gating dynamically selects and recombines features based on context, addressing the limitations of RobustSIRR’s static concatenation and RDNet’s fixed reversible paths. This enables flexible cross-scale coordination that prevents progressive degradation and establishes well-structured representations for LFSB’s layer disentanglement. At Levels $\{1, 0\}$, due to the absence of extracted global feature \mathbf{P}_ℓ , we simply use $\mathbf{F}_\ell = \mathbf{F}_{\ell+1} + \mathbf{E}_\ell$ for feature aggregation.

3.2. Layer Fusion-Separation Block

Complementary to CrGF’s global feature flow, explicit *intra-layer disentanglement* is critical for preventing transmission-reflection confusion. However, existing methods lack effective separation mechanisms: DSRNet [13] uses MuGI without attention-based separation;

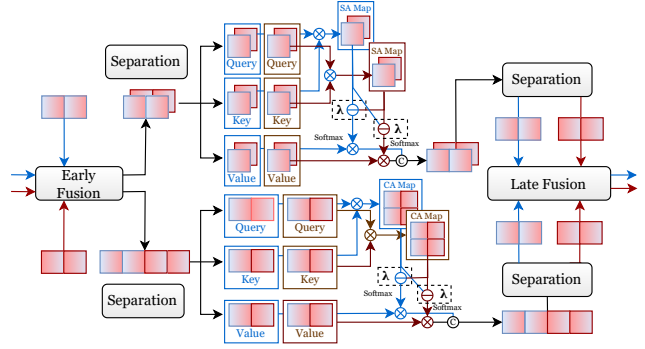


Figure 5. **Layer Fusion-Separation Block (LFSB).** LFSB alternates between fusion (shared structure) and separation (layer disentanglement): (1) Bidirectional projection aligns transmission-reflection features; (2) Dual-dimensional attention (SA + CA) models spatial and inter-layer dependencies; (3) Differential operators $\mathbf{A}^t - \lambda_\ell \mathbf{A}^r$ suppress cross-stream interference; (4) FFNs with residuals integrate separated features.

RDNet [43] preserves flow via reversibility but lacks explicit complementarity modeling; DSIT [14] aggregates dual-dimensional attention without separation constraints, causing progressive feature confusion (Figure 2).

To address these limitations, we propose LFSB (Figure 5), which alternates between two complementary operations—fusion for extracting shared structure and differential dual-dimensional attention for enforcing layer-specific disentanglement.

Early Fusion. Before applying attention, we align semantic spaces via bidirectional cross-stream projection to establish a foundation for effective layer interaction. At decoder stage ℓ , given $\mathbf{F}_\ell^t, \mathbf{F}_\ell^r \in \mathbb{R}^{H_\ell \times W_\ell \times C}$:

$$\mathbf{F}_\ell^{t'} = \mathbf{W}^t[\mathbf{F}_\ell^t \parallel \mathbf{F}_\ell^r], \quad \mathbf{F}_\ell^{r'} = \mathbf{W}^r[\mathbf{F}_\ell^r \parallel \mathbf{F}_\ell^t], \quad (4)$$

where $\mathbf{W}^t, \mathbf{W}^r \in \mathbb{R}^{C \times 2C}$ extract shared degradation patterns between transmission and reflection layers, enabling each stream to benefit from complementary cues before feature separation. This bidirectional projection explicitly aligns feature spaces, preparing well-structured representations for subsequent differential attention computation.

Differential Dual-Dimensional Attention. Following DSIT [14], we employ dual-dimensional attention to jointly model intra-layer spatial correlations and inter-layer complementarity after window-partitioning. Inspired by Differential Transformer [41] that suppresses noise through attention cancellation in single-stream architectures, we extend this principle to dual-stream layer separation by introducing differential operators across transmission and reflection branches. However, unlike Differential Transformer that computes $\text{Attn}_{\text{diff}} = \text{softmax}(\mathbf{Q}\mathbf{K}^\top / \sqrt{d}) - \lambda \cdot$

$\text{softmax}(\mathbf{Q}\mathbf{K}^\top/\sqrt{d})$ within the same attention head to cancel noise patterns, our method performs cross-stream subtraction $\mathbf{A}^t - \lambda_\ell \mathbf{A}^r$ to suppress inter-layer interference between complementary transmission and reflection features.

We concatenate features along the batch dimension for self-attention (SA) $\mathbf{F}_{\text{SA}} = \text{concat}([\mathbf{F}_\ell^t, \mathbf{F}_\ell^{r'}]) \in \mathbb{R}^{2B \times N \times C}$, computing independent attention maps $\mathbf{A}_{\text{SA}}^t, \mathbf{A}_{\text{SA}}^r$ for spatial refinement. Complementarily, we concatenate along the sequence dimension for cross-attention (CA) $\mathbf{F}_{\text{CA}} = \text{concat}([\mathbf{F}_\ell^t, \mathbf{F}_\ell^{r'}]) \in \mathbb{R}^{B \times 2N \times C}$, capturing inter-layer dependencies via $\mathbf{A}_{\text{CA}}^t, \mathbf{A}_{\text{CA}}^r$.

Afterwards, unlike DSIT that directly aggregates SA and CA outputs, we introduce differential operators to actively suppress cross-stream interference:

$$\begin{aligned} \mathbf{A}_{\text{diff}}^t &= (\mathbf{A}_{\text{SA}}^t + \mathbf{A}_{\text{CA}}^t) - \sigma(\lambda_\ell)(\mathbf{A}_{\text{SA}}^r + \mathbf{A}_{\text{CA}}^r); \\ \mathbf{A}_{\text{diff}}^r &= (\mathbf{A}_{\text{SA}}^r + \mathbf{A}_{\text{CA}}^r) - \sigma(\lambda_\ell)(\mathbf{A}_{\text{SA}}^t + \mathbf{A}_{\text{CA}}^t), \end{aligned} \quad (5)$$

where learnable λ_ℓ in $[0, 1]$, controls differential strength and $\sigma(\cdot)$ is sigmoid function. This cross-stream subtraction $-\sigma(\lambda_\ell)\mathbf{A}^r$ ensures transmission-specific and reflection-specific features remain distinguishable throughout decoder stages, addressing the progressive feature confusion. As shown in Figure 6, this differential mechanism effectively separates layer-specific attention patterns by distributing attention across multiple heads, reducing noisy activations and enabling clearer distinction between transmission and reflection features.

Late Fusion & Aggregation. The separated attention features are integrated via feed-forward refinement with residual connections:

$$\mathbf{F}_{\ell+1}^t = \mathbf{F}_\ell^t + \text{FFN}(\mathbf{A}_{\text{diff}}^t), \quad \mathbf{F}_{\ell+1}^r = \mathbf{F}_\ell^r + \text{FFN}(\mathbf{A}_{\text{diff}}^r), \quad (6)$$

stabilizing gradient propagation across decoder depths. Combined with our stage-wise curriculum training (Section 3.3), this explicit fusion-separation paradigm maintains clear transmission-reflection distinction throughout the network hierarchy.

3.3. Curriculum Training and Loss Function

LFSB’s differential separation relies on λ_ℓ to suppress cross-stream interference via $\mathbf{A}^t - \sigma(\lambda_\ell)\mathbf{A}^r$. However, λ requires careful control: excessive strength in early training destabilizes poorly-structured features, while insufficient strength fails to enforce separation, causing confusion. We adopt curriculum learning [17] to progressively strengthen differential separation, enabling the network to learn shared structure before refining layer-specific features, through two complementary mechanisms.

Depth-Dependent Initialization. Different decoder depths require different separation strengths. For LFSB at decoder layer ℓ :

$$\lambda_\ell^{\text{init}} = 0.8 - 0.6 e^{-0.3\ell}, \quad (7)$$

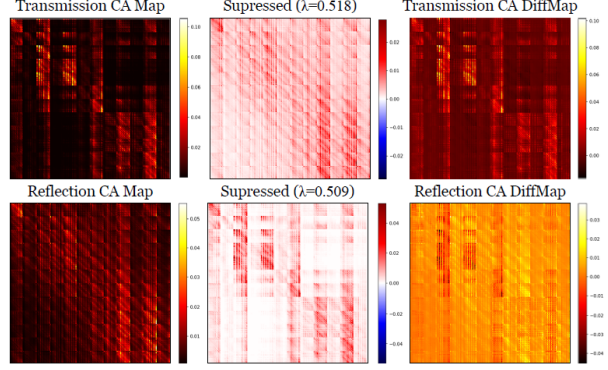


Figure 6. **Differential attention visualization.** Cross-attention maps reveal overlapping patterns between transmission and reflection (left). Differential separation via $\mathbf{A}^t - \sigma(\lambda_\ell)\mathbf{A}^r$ actively suppresses cross-stream interference (middle), producing balanced, layer-specific attention distributions (right) that enable effective feature disentanglement.

where deeper layers receive stronger weights ($\lambda \rightarrow 0.8$) for global separation, while shallow layers maintain weaker weights ($\lambda \rightarrow 0.2$) to preserve fine-grained details.

Epoch-Wise Warmup. To stabilize training, we gradually increase the differential separation strength across epochs. At epoch $e \in \{1, \dots, E_{\text{total}}\}$, the global scaling factor is:

$$\lambda_{\text{diff}}(e) = \begin{cases} 0.1 + 0.9 \frac{e}{E_{\text{warmup}}}, & e < E_{\text{warmup}}, \\ 1.0, & e \geq E_{\text{warmup}}, \end{cases} \quad (8)$$

where $E_{\text{warmup}} = 30$ is the warmup period. This schedule linearly increases $\lambda_{\text{diff}}(e)$ from 0.1 to 1.0 during the first 30 epochs, then maintains full strength thereafter. The final effective coefficient combines spatial (depth-dependent) and temporal (epoch-wise) adaptation:

$$\lambda_\ell(e) = \lambda_\ell^{\text{init}} \cdot \lambda_{\text{diff}}(e). \quad (9)$$

Early training prioritizes holistic reconstruction with weak differential constraints, while later stages enforce strong layer-specific separation.

Loss Functions. Let $\hat{\mathbf{T}}$, $\hat{\mathbf{R}}$, and $\hat{\mathbf{R}}\mathbf{R}$ denote predicted transmission, reflection, and residual layers, with \mathbf{T} , \mathbf{R} as ground truth. The training objective is:

$$\begin{aligned} \mathcal{L}_{\text{total}} &= \lambda_{\text{rec}} \mathcal{L}_{\text{rec}} + \lambda_{\text{refl}} \mathcal{L}_{\text{refl}} + \lambda_{\text{vgg}} \mathcal{L}_{\text{vgg}} + \lambda_{\text{color}} \mathcal{L}_{\text{color}} \\ &\quad + \lambda_{\text{exclu}} \mathcal{L}_{\text{exclu}} + \lambda_{\text{recons}} \mathcal{L}_{\text{recons}}, \end{aligned} \quad (10)$$

where we use Charbonnier loss [2] $\mathcal{L}_{\text{rec}} = \sqrt{\|\hat{\mathbf{T}} - \mathbf{T}\|^2 + \epsilon^2}$ ($\epsilon = 10^{-6}$) and ℓ_1 loss $\mathcal{L}_{\text{refl}} = \|\hat{\mathbf{R}} - \mathbf{R}\|_1$ for pixel-wise supervision. \mathcal{L}_{vgg} is VGG perceptual loss [27] using features from layers $\{2, 7, 12, 21, 30\}$. $\mathcal{L}_{\text{color}}$ is color consistency loss for output’s reflection color

Table 1. **Quantitative comparisons on synthetic datasets.** We evaluate on Real20, Nature, and three subsets of SIR² [31] (Objects, Postcard, Wild). Best, second-best, and third-best results are highlighted in red, orange, and yellow respectively.

Methods	Venue	Trainable Parameters	Real20 (20)		Objects (200)		Postcard (199)		Wild (101)		Nature (20)		Average (540)	
			PSNR↑	SSIM↑	PSNR↑	SSIM↑	PSNR↑	SSIM↑	PSNR↑	SSIM↑	PSNR↑	SSIM↑	PSNR↑	SSIM↑
Zhang et al. [42]	CVPR 2018	3.1M	21.36	0.776	24.27	0.889	22.89	0.877	24.82	0.898	22.00	0.779	23.67	0.878
ERRNet [36]	CVPR 2019	28.8M	22.69	0.803	24.10	0.891	20.78	0.836	25.33	0.903	23.08	0.800	23.01	0.866
IBCLN [21]	CVPR 2020	24.3M	19.42	0.750	24.01	0.884	22.77	0.871	23.52	0.878	20.68	0.763	23.17	0.869
Zheng et al. [44]	CVPR 2021	38.4M	18.07	0.694	22.48	0.813	19.65	0.819	19.99	0.798	18.40	0.690	20.66	0.803
YTMT [12]	NeurIPS 2021	29.9M	23.01	0.810	25.03	0.898	22.32	0.864	24.95	0.888	24.13	0.818	23.91	0.877
DSRNet [13]	ICCV 2023	123.6M	24.19	0.821	26.74	0.921	24.46	0.904	26.52	0.922	25.61	0.844	25.72	0.908
Zhong et al. [45]	CVPR 2024	–	24.05	0.824	26.51	0.927	25.02	0.915	26.23	0.925	23.87	0.812	25.72	0.914
MaxRF [47]	CVPR 2024	27.9M	21.58	0.794	25.80	0.915	21.45	0.863	26.35	0.924	25.58	0.837	24.14	0.890
DSIT [14]	NeurIPS 2024	136M	24.71	0.831	26.77	0.921	24.47	0.910	27.11	0.925	26.61	0.844	25.93	0.886
DExNet [15]	TPAMI 2025	9.6M	23.42	0.816	25.37	0.909	24.21	0.906	26.65	0.922	23.39	0.828	25.04	0.904
RDNet [43]	CVPR 2025	266.4M	25.17	0.841	27.11	0.925	25.04	0.910	27.86	0.931	26.75	0.846	26.38	0.890
ReflexSplit (Ours)	–	174M	25.22	0.846	27.08	0.929	25.38	0.927	27.30	0.933	27.03	0.854	26.40	0.898

enhancement. $\mathcal{L}_{\text{exclu}}$ is exclusion loss [42] encouraging gradient orthogonality between layers:

$$\mathcal{L}_{\text{exclu}} = \sum_{l=1}^3 \left(\|\nabla_x \hat{\mathbf{T}} \odot \nabla_x \hat{\mathbf{R}}\|_1 + \|\nabla_y \hat{\mathbf{T}} \odot \nabla_y \hat{\mathbf{R}}\|_1 \right), \quad (11)$$

where ∇_x, ∇_y are spatial gradients and \odot is element-wise product. $\mathcal{L}_{\text{recons}} = \|\hat{\mathbf{T}} + \hat{\mathbf{R}} + \hat{\mathbf{R}}\mathbf{R} - \mathbf{I}\|_1$ enforces reconstruction consistency. Color consistency loss $\mathcal{L}_{\text{color}} = \|\mu(\hat{\mathbf{R}}) - \mu(\mathbf{R})\|_1 + \|\sigma(\hat{\mathbf{R}}) - \sigma(\mathbf{R})\|_1$, is enforced to maintain color fidelity in the separated reflection layer. We set $\lambda_{\text{rec}} = 1.0$, $\lambda_{\text{refl}} = 0.5$, $\lambda_{\text{vgg}} = 0.1$, $\lambda_{\text{exclu}} = 1.0$, $\lambda_{\text{recons}} = 0.2$. As $\lambda_{\text{diff}}(e)$ increases during training, the model shifts from holistic reconstruction to differential refinement.

4. Experiment Results

Dataset and Implementation Details. We train on a composite dataset comprising 7,643 synthetic pairs from PASCAL VOC [4], 90 real pairs from [42], and 200 pairs from Nature [21]. For synthetic data, transmission and reflection layers are randomly sampled from PASCAL VOC and blended following the nonlinear model inspired by the “screen” blending mode in digital image processing [13]:

$$\mathbf{I}_{\text{syn}} = \gamma_1 \mathbf{T}_{\text{syn}} + \gamma_2 \mathbf{R}_{\text{syn}} - \gamma_1 \gamma_2 \mathbf{T}_{\text{syn}} \circ \mathbf{R}_{\text{syn}}, \quad (12)$$

where $\mathbf{T}_{\text{syn}}, \mathbf{R}_{\text{syn}}$, and \mathbf{I}_{syn} represent transmission, reflection, and superimposed layers during synthesis, respectively. The attenuation coefficients are randomly sampled as $\gamma_1 \in [0.8, 1.0]$ and $\gamma_2 \in [0.4, 1.0]$ to simulate varying layer intensities. This formulation reserves lighter colors for the blending layers, effectively modeling real-world nonlinear mixing phenomena such as over-exposure and specular highlights. Each epoch samples 5,000 pairs with distribution ratio 0.6 : 0.2 : 0.2 (synthetic:real:Nature).

For evaluation, we use five benchmarks: Real20 (20 images), Nature (20 images), and three SIR² subsets [31]—Objects (200), Postcard (199), and Wild (101). We also

Table 2. **Cross-dataset evaluation on OpenRR-1K [40].** ReflexSplit achieves highest SSIM and lowest LPIPS, demonstrating superior perceptual quality and generalization capability.

Methods	PSNR↑	SSIM↑	LPIPS↓	NIQE↓	DISTS↓
DSRNet [13]	24.5228	0.9139	0.1350	3.0109	0.0865
MaxRF [47]	24.3146	0.9056	0.1180	3.2317	0.0750
DExNet [15]	26.1434	0.9351	0.1189	3.1006	0.0766
DSIT [14]	26.6672	0.9341	0.1137	2.9872	0.0700
RDNet [43]	24.9297	0.9271	0.1140	3.1906	0.0728
ReflexSplit (Ours)	26.5824	0.9372	0.1087	2.9764	0.0684

evaluate on the real-world OpenRR-1K dataset [40]. All images are resized to 384×384 during training. The model is implemented in PyTorch and optimized using Adam with learning rate = 10^{-4} , weight decay = 0, and batch size = 1. We apply CosineAnnealingLR scheduling ($T_{\text{max}} = 10$, $\eta_{\text{min}} = 8 \times 10^{-6}$) and train for 200 epochs. For LFSB, we set window size $W = 12$, number of attention heads $H = \{2, 4, 8, 8, 8\}$ at decoder levels $\{0, 2, 3, 4, 5\}$ respectively, and the differential warmup period $E_{\text{warmup}} = 30$ epochs. All experiments are conducted on a NVIDIA RTX 4090 GPU and are based on their original settings.

4.1. Quantitative Comparison

We evaluate ReflexSplit against eleven state-of-the-art methods: Zhang et al. [42], ERRNet [36], IBCLN [21], Zheng et al. [44], YTMT [12], DSRNet [13], Zhong et al. [45], MaxRF [47], DSIT [14], DExNet [15], and RDNet [43] on synthetic and real-world benchmarks.

Synthetic Benchmarks. Table 1 presents quantitative results across five synthetic datasets. The consistent SSIM leadership demonstrates ReflexSplit’s superior perceptual quality through explicit layer separation, while competitive PSNR scores validate reconstruction fidelity. Notably, our method achieves this with 174M parameters—34% fewer than RDNet and 28% more than DSIT, offering an effective balance between performance and efficiency.

Real-World Benchmarks and Cross-Dataset Generalization. On OpenRR-1K (Table 2), we evaluate cross-

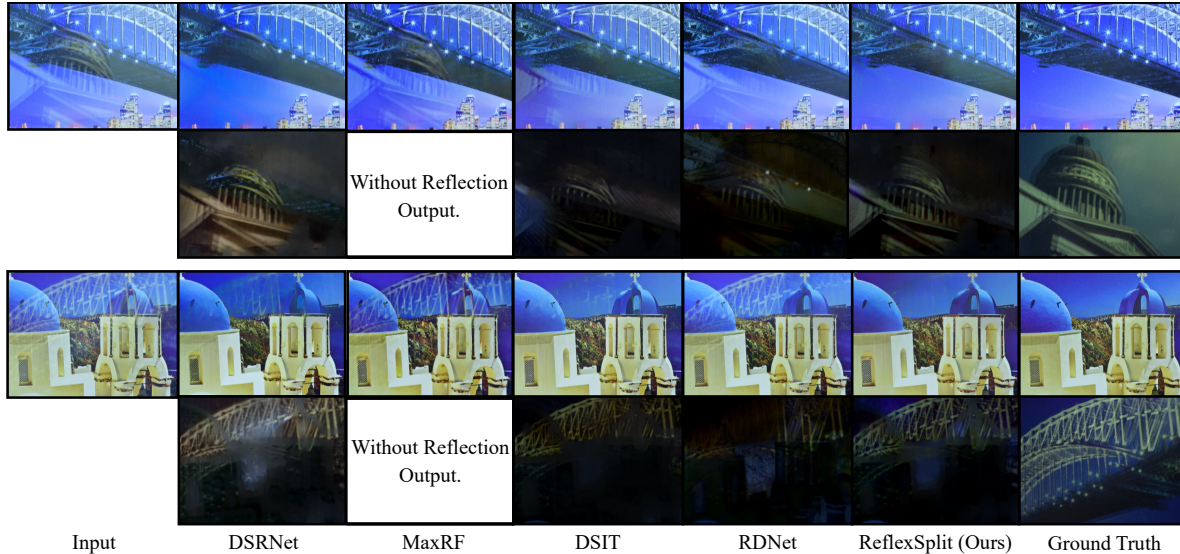


Figure 7. **Qualitative comparison on Postcard [31]**. ReflexSplit achieves superior reflection separation and detail preservation.

dataset generalization by directly testing models trained on PASCAL VOC [4], Real20, and Nature without fine-tuning. We adopt both full-reference (PSNR/SSIM/LPIPS) and no-reference metrics (NIQE/DISTS) for comprehensive quality assessment. ReflexSplit achieves the highest SSIM and lowest LPIPS, demonstrating superior perceptual quality and structural fidelity on unseen real-world data. While DSIT obtains marginally higher PSNR, our method excels in perceptual metrics, indicating better preservation of fine-grained details and natural texture without over-smoothing.

4.2. Qualitative Comparison

We compare ReflexSplit against DSRNet [13], MaxRF [47], DSIT [14], and RDNet [43] on Postcard, Wild, and SolidObject datasets.

As shown in Figures 7–8, competing methods exhibit distinct limitations: DSIT suffers transmission-reflection confusion; DSRNet fails in high-frequency regions; RDNet introduces color distortion; MaxRF loses edge details. ReflexSplit produces cleaner separation across diverse scenarios, preserving fine-grained textures, boundaries, and color fidelity. This results from CrGF maintaining hierarchical consistency through adaptive aggregation and LFSB preventing feature confusion via explicit fusion-separation.

4.3. Ablation Study

We conduct ablation studies to validate each component’s contribution using identical training settings described in Section 4. All variants are trained for 200 epochs on the composite dataset and evaluated on Real20 and SIR² benchmarks.

Effect of CrGF. CrGF is critical for hierarchical feature

consistency. Table 3 shows that CrGF substantially outperforms alternative fusion strategies—direct aggregation, concatenation, and element-wise addition—demonstrating the importance of bidirectional gating for adaptive multi-scale coordination. This validates that stable separation requires both cross-scale aggregation (CrGF) and layer disentanglement (LFSB).

Effect of LFSB Components. Table 4 and Figure 9 validate each component’s contribution through progressive ablation. The baseline dual-stream decoder without explicit interaction suffers from severe transmission-reflection confusion. Bidirectional cross-stream projection in early fusion substantially improves performance by aligning semantic spaces, establishing a foundation for effective interaction. Building upon early fusion, self-attention captures intra-layer spatial correlations independently for each stream, while cross-attention enables explicit inter-layer information exchange. However, simply aggregating SA and CA outputs risks reinforcing shared patterns rather than separating layers. The key innovation is introducing differential operators ($\mathbf{A}^t - \lambda \mathbf{A}^r$) that actively suppress cross-stream interference, preventing progressive feature entanglement. As shown in Figure 9, removing LFSB causes PSNR to drop to 19.946 and Normalized Cross-Correlation (NCC, measuring inter-stream similarity where lower is better) to 0.9254, confirming its critical role in layer separation.

Effect of Training Strategy. Table 5 validates our curriculum training: fixed strength causes instability, single-stage scheduling underperforms, while our full strategy combining both achieves optimal convergence by progressively adapting across spatial and temporal dimensions.

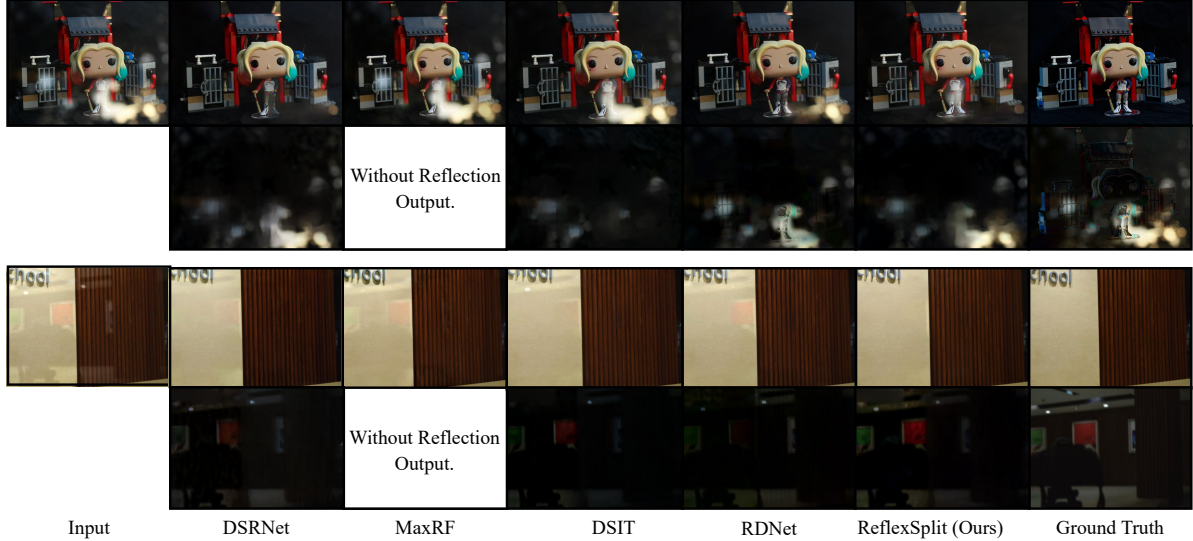


Figure 8. **Qualitative comparison on Real20 and Wild [31].** ReflexSplit achieves superior reflection suppression while preserving fine-grained textures and color fidelity. Competing methods exhibit residual reflections, over-smoothing, or color distortion.

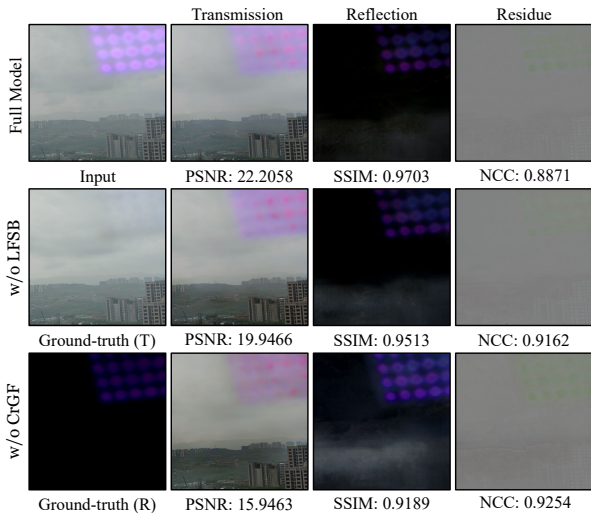


Figure 9. **Ablation study on challenging example.** Removing CrGF causes catastrophic failure, while removing LFSB leads to layer confusion. Both are essential for stable separation.

Table 3. **Ablation study on CrGF.** We compare our Cross-scale Gated Fusion against alternative fusion strategies. All experiments use identical training settings.

Fusion Strategy	Real20		SIR ²		Nature	
	PSNR \uparrow	SSIM \uparrow	PSNR \uparrow	SSIM \uparrow	PSNR \uparrow	SSIM \uparrow
(a) No Fusion (Direct Aggregation)	24.01	0.838	25.32	0.881	25.84	0.832
(b) Simple Concatenation	24.89	0.828	25.67	0.878	26.21	0.841
(c) Element-wise Addition	25.01	0.830	25.78	0.883	26.45	0.846
(d) CrGF (Ours)	25.22	0.846	26.33	0.896	27.03	0.854

5. Conclusion

We present ReflexSplit, a dual-stream framework that addresses transmission-reflection confusion in SIRS through

Table 4. **Ablation study on LFSB components.** We progressively add each component to evaluate its contribution.

Variant	Early Fusion	SA Only	SA+CA	Diff Sep	Late Fusion	Real20	
						PSNR \uparrow	SSIM \uparrow
(a) Baseline	\times	\times	\times	\times	\times	23.87	0.812
(b) + Early Fusion	\checkmark	\times	\times	\times	\times	24.32	0.823
(c) + SA	\checkmark	\checkmark	\times	\times	\times	24.61	0.831
(d) + SA + CA	\checkmark	\times	\checkmark	\times	\times	24.89	0.838
(e) + Diff Sep	\checkmark	\times	\checkmark	\checkmark	\times	25.08	0.842
(f) Full LFSB (Ours)	\checkmark	\times	\checkmark	\checkmark	\checkmark	25.22	0.846

Table 5. **Ablation on training strategy.** The full curriculum strategy achieves the best performance, confirming the effectiveness of both depth-dependent initialization and epoch-wise warmup.

Strategy	Real20		SIR ²	
	PSNR \uparrow	SSIM \uparrow	PSNR \uparrow	SSIM \uparrow
Fixed λ (= 0.5)	24.83	0.821	25.89	0.883
Warmup only	24.95	0.835	26.11	0.891
Depth-init only	25.08	0.840	26.18	0.889
Full strategy (Ours)	25.22	0.846	26.33	0.896

explicit layer fusion-separation. Our approach integrates three key innovations: Cross-scale Gated Fusion (CrGF) adaptively aggregates multi-scale features across decoder depths, stabilizing gradient flow and maintaining hierarchical consistency; Layer Fusion-Separation Blocks (LFSB) alternate between fusion for shared structure extraction and differential separation for layer-specific disentanglement via cross-stream attention subtraction; curriculum training progressively strengthens differential separation through depth-dependent initialization and epoch-wise warmup. This synergistic design prevents progressive feature entanglement that plagues existing methods. Extensive experiments on synthetic and real-world benchmarks demonstrate state-of-the-art performance with superior perceptual quality and robust generalization.

ReflexSplit: Single Image Reflection Separation via Layer Fusion-Separation

Supplementary Material

Overview

This supplementary material provides comprehensive details to support the main paper. The document is organized as follows:

- **Section 1: Algorithm Description** – Complete algorithmic specification of the ReflexSplit training pipeline, including dual-branch feature extraction, hierarchical decoding with CrGF and LFSB, and curriculum learning strategy.
- **Section 2: Loss Functions Details** – Detailed formulation of all loss components: reconstruction losses, perceptual loss, exclusion loss, reconstruction consistency, and color consistency loss with weight configurations.
- **Section 3: Feature Separation Analysis with DSIT** – t-SNE and PCA analysis comparing progressive disentanglement strategy of ReflexSplit against immediate separation approach of DSIT, demonstrating more distributed feature representations and curriculum-based layer learning.
- **Section 4: Comparison with RDNet on Real-World Scenarios** – Performance comparison with RDNet on OpenRR-1K, showing ReflexSplit achieves improvements on 63% of test images. Discussion of complementary architectural philosophies between reversible designs and explicit layer separation approaches.
- **Section 5: Additional Visual Comparisons** – Extensive qualitative results on OpenRR-1K and SIR² datasets, demonstrating reflection suppression, color fidelity, and detail preservation compared to state-of-the-art methods.
- **Section 6: Failure Cases and Limitations** – Analysis of challenging scenarios where ReflexSplit struggles: complex outdoor lighting, specular reflections, and mixed indoor-outdoor scenes with extreme brightness differences.
- **Section 7: Network Architecture Details** – Complete architecture specification with layer-by-layer breakdown of dual-branch encoders, feature mixing, hierarchical decoder stages, and output generation modules.
- **Section 8: More Complexity Comparison** – We present a comprehensive efficiency analysis comparing ReflexSplit with existing methods, demonstrating its practical advantage as a single-stage solution with competitive computational cost.

6. Algorithm Description

We provide a detailed algorithmic description of ReflexSplit in Algorithm 1, which illustrates the complete training

Algorithm 1 ReflexSplit Training Algorithm

Require: Mixed image $\mathbf{I} \in \mathbb{R}^{H \times W \times 3}$, ground truth transmission \mathbf{T} and reflection \mathbf{R} , training epoch e , warmup epoch E_{warmup}

Ensure: Predicted transmission $\hat{\mathbf{T}}$, reflection $\hat{\mathbf{R}}$, and residual $\hat{\mathbf{R}}\hat{\mathbf{R}}$

- 1: // Stage 1: Dual-Branch Feature Extraction
- 2: Extract global semantic priors via Swin Transformer:
- 3: $\{\mathbf{P}_2, \mathbf{P}_3, \mathbf{P}_4, \mathbf{P}_5\} \leftarrow \text{GFEB}(\mathbf{I})$
- 4: Extract local texture features via MuGI-CNN:
- 5: $\{\mathbf{E}_0, \mathbf{E}_1, \mathbf{E}_2, \mathbf{E}_3, \mathbf{E}_4, \mathbf{E}_5\} \leftarrow \text{LFEB}(\mathbf{I})$
- 6: // Stage 2: Hierarchical Decoding with CrGF and LFSB
- 7: for decoder level $\ell = 5$ to 0 do
- 8: if $\ell \in \{4, 3, 2\}$ then
- 9: // Cross-scale Gated Fusion (CrGF)
- 10: $\mathbf{F}_\ell^{\text{raw}} \leftarrow \mathbf{F}_{\ell+1} + \mathbf{P}_\ell + \mathbf{E}_\ell$
- 11: Compute bidirectional gating:
- 12: $\mathbf{F}_\ell^{\text{main}} = \mathcal{G}_1(\mathbf{F}_\ell^{\text{raw}}) \odot \mathcal{G}_2(\mathbf{F}_{\ell+1})$
- 13: $\mathbf{F}_\ell^{\text{aux}} = \mathcal{G}_1(\mathbf{F}_{\ell+1}) \odot \mathcal{G}_2(\mathbf{F}_\ell^{\text{raw}})$
- 14: $\mathbf{F}_\ell^{\text{fused}} = w_\ell^{(1)} \phi_1(\mathbf{F}_\ell^{\text{main}}) + w_\ell^{(2)} \phi_2(\mathbf{F}_\ell^{\text{aux}})$
- 15: else
- 16: // Direct Aggregation
- 17: $\mathbf{F}_\ell^{\text{fused}} \leftarrow \mathbf{F}_{\ell+1} + \mathbf{E}_\ell$
- 18: end if
- 19: // Layer Fusion-Separation Block (LFSB)
- 20: /* Early Fusion: Bidirectional Projection */
- 21: $\mathbf{F}_\ell^{t'} = \mathbf{W}^t[\mathbf{F}_\ell^t \parallel \mathbf{F}_\ell^r]$
- 22: $\mathbf{F}_\ell^{r'} = \mathbf{W}^r[\mathbf{F}_\ell^t \parallel \mathbf{F}_\ell^r]$
- 23: /* Differential Dual-Dimensional Attention */
- 24: Compute self-attention (batch-wise):
- 25: $\mathbf{A}_{\text{SA}}^t, \mathbf{A}_{\text{SA}}^r \leftarrow \text{SA}(\text{concat}([\mathbf{F}_\ell^{t'}, \mathbf{F}_\ell^{r'}], \text{dim} = 0))$
- 26: Compute cross-attention (sequence-wise):
- 27: $\mathbf{A}_{\text{CA}}^t, \mathbf{A}_{\text{CA}}^r \leftarrow \text{CA}(\text{concat}([\mathbf{F}_\ell^{t'}, \mathbf{F}_\ell^{r'}], \text{dim} = 1))$
- 28: /* Differential Separation with Curriculum */
- 29: Compute depth-dependent weight:
- 30: $\lambda_\ell^{\text{init}} = 0.8 - 0.6 \exp(-0.3\ell)$
- 31: Compute epoch-wise warmup:
- 32:
$$\lambda_{\text{diff}}(e) = \begin{cases} 0.1 + 0.9 \frac{e}{E_{\text{warmup}}}, & e < E_{\text{warmup}} \\ 1.0, & e \geq E_{\text{warmup}} \end{cases}$$
- 33: $\lambda_\ell(e) \leftarrow \lambda_\ell^{\text{init}} \cdot \lambda_{\text{diff}}(e)$
- 34: Apply differential operators:
- 35: $\mathbf{A}_{\text{diff}}^t = (\mathbf{A}_{\text{SA}}^t + \mathbf{A}_{\text{CA}}^t) - \sigma(\lambda_\ell)(\mathbf{A}_{\text{SA}}^r + \mathbf{A}_{\text{CA}}^r)$
- 36: $\mathbf{A}_{\text{diff}}^r = (\mathbf{A}_{\text{SA}}^r + \mathbf{A}_{\text{CA}}^r) - \sigma(\lambda_\ell)(\mathbf{A}_{\text{SA}}^t + \mathbf{A}_{\text{CA}}^t)$
- 37: /* Late Fusion: FFN with Residual */
- 38: $\mathbf{F}_{\ell+1}^t = \mathbf{F}_\ell^t + \text{FFN}(\mathbf{A}_{\text{diff}}^t)$
- 39: $\mathbf{F}_{\ell+1}^r = \mathbf{F}_\ell^r + \text{FFN}(\mathbf{A}_{\text{diff}}^r)$
- 40: end for
- 41: // Stage 3: Output Generation
- 42: $\hat{\mathbf{T}}, \hat{\mathbf{R}} \leftarrow \text{Conv}_{3 \times 3}(\mathbf{F}_0^t), \text{Conv}_{3 \times 3}(\mathbf{F}_0^r)$
- 43: $\hat{\mathbf{R}}\hat{\mathbf{R}} \leftarrow \text{LRM}(\mathbf{F}_0^t + \mathbf{F}_0^r)$
- 44: // Loss Computation
- 45: $\mathcal{L}_{\text{total}} = \lambda_{\text{rec}}\mathcal{L}_{\text{rec}} + \lambda_{\text{refl}}\mathcal{L}_{\text{refl}} + \lambda_{\text{vgg}}\mathcal{L}_{\text{vgg}}$
- 46: $+ \lambda_{\text{exclu}}\mathcal{L}_{\text{exclu}} + \lambda_{\text{recons}}\mathcal{L}_{\text{recons}} + \lambda_{\text{color}}\mathcal{L}_{\text{color}}$
- 47: return $\hat{\mathbf{T}}, \hat{\mathbf{R}}, \hat{\mathbf{R}}\hat{\mathbf{R}}$

pipeline including dual-branch feature extraction, hierarchical decoding with CrGF and LFSB, and curriculum learning strategy.

7. Loss Functions Details

Let $\hat{\mathbf{T}}$, $\hat{\mathbf{R}}$, and $\hat{\mathbf{R}}\hat{\mathbf{R}}$ denote the predicted transmission, reflection, and residual layers, respectively, with \mathbf{T} and \mathbf{R} as ground truth. Our training objective combines multiple complementary loss terms:

$$\begin{aligned} \mathcal{L}_{\text{total}} = & \lambda_{\text{rec}} \mathcal{L}_{\text{rec}} + \lambda_{\text{refl}} \mathcal{L}_{\text{refl}} + \lambda_{\text{vgg}} \mathcal{L}_{\text{vgg}} \\ & + \lambda_{\text{exclu}} \mathcal{L}_{\text{exclu}} + \lambda_{\text{recons}} \mathcal{L}_{\text{recons}} + \lambda_{\text{color}} \mathcal{L}_{\text{color}}. \end{aligned} \quad (13)$$

Reconstruction losses. For transmission layer reconstruction, we employ Charbonnier loss [2] to handle outliers robustly:

$$\mathcal{L}_{\text{rec}} = \sqrt{\|\hat{\mathbf{T}} - \mathbf{T}\|^2 + \epsilon^2}, \quad \epsilon = 10^{-3}. \quad (14)$$

For reflection layer supervision, we use ℓ_1 loss:

$$\mathcal{L}_{\text{refl}} = \|\hat{\mathbf{R}} - \mathbf{R}\|_1. \quad (15)$$

Perceptual loss. To preserve semantic content and texture details, we adopt VGG perceptual loss [27] using features extracted from layers $\{2, 7, 12, 21, 30\}$ of a pretrained VGG-19 network:

$$\mathcal{L}_{\text{vgg}} = \sum_{i \in \{2, 7, 12, 21, 30\}} w_i \cdot \|\phi_i(\hat{\mathbf{T}}) - \phi_i(\mathbf{T})\|_1, \quad (16)$$

where $\phi_i(\cdot)$ denotes the feature extractor at layer i and w_i are weights balancing contributions across layers.

Exclusion loss. Following [42], we enforce gradient orthogonality between transmission and reflection to encourage layer independence:

$$\mathcal{L}_{\text{exclu}} = \sum_{l=1}^3 \left(\|\nabla_x \hat{\mathbf{T}} \odot \nabla_x \hat{\mathbf{R}}\|_1 + \|\nabla_y \hat{\mathbf{T}} \odot \nabla_y \hat{\mathbf{R}}\|_1 \right), \quad (17)$$

where ∇_x and ∇_y denote spatial gradients along horizontal and vertical directions, and \odot represents element-wise multiplication. This term penalizes overlapping gradient patterns, thereby promoting structural separation between layers.

Reconstruction consistency. To ensure the decomposed layers reconstruct the input accurately, we enforce:

$$\mathcal{L}_{\text{recons}} = \|\hat{\mathbf{T}} + \hat{\mathbf{R}} + \hat{\mathbf{R}}\hat{\mathbf{R}} - \mathbf{I}\|_1, \quad (18)$$

where \mathbf{I} is the input mixed image. This constraint guarantees that no information is lost during decomposition.

Color consistency loss. To maintain color fidelity in the separated reflection layer, we introduce a color consistency term that matches color statistics between prediction and ground truth:

$$\mathcal{L}_{\text{color}} = \|\mu(\hat{\mathbf{R}}) - \mu(\mathbf{R})\|_1 + \|\sigma(\hat{\mathbf{R}}) - \sigma(\mathbf{R})\|_1, \quad (19)$$

Table 6. **Performance margin distribution on OpenRR-1K.** Comparison of ReflexSplit against RDNet [43] on both test and validation splits. $\Delta_{\text{PSNR}} = \text{PSNR}_{\text{Ours}} - \text{PSNR}_{\text{RDNet}}$.

Condition	Test Set (99 images)		Val Set (100 images)	
	Count	Percentage	Count	Percentage
$\Delta_{\text{PSNR}} > 0$ dB	63 / 99	63.64%	62 / 100	62.00%
$\Delta_{\text{PSNR}} > 3$ dB	20 / 99	20.20%	18 / 100	18.00%
$\Delta_{\text{PSNR}} > 5$ dB	8 / 99	8.08%	10 / 100	10.00%
$\Delta_{\text{PSNR}} > 7$ dB	5 / 99	5.05%	4 / 100	4.00%

where $\mu(\cdot)$ and $\sigma(\cdot)$ compute channel-wise mean and standard deviation.

Loss weights. We set the loss weights as: $\lambda_{\text{rec}} = 1.0$, $\lambda_{\text{refl}} = 0.5$, $\lambda_{\text{vgg}} = 0.1$, $\lambda_{\text{exclu}} = 1.0$, $\lambda_{\text{recons}} = 0.2$, and $\lambda_{\text{color}} = 0.1$.

8. Feature Separation Analysis: Comparison with DSIT

DSIT [14] represents a strong baseline with its dual-stream transformer architecture. However, we observe that different separation strategies may lead to distinct feature learning behaviors under complex real-world mixing conditions.

Figures 10 and 11 provide feature space analysis comparing ReflexSplit and DSIT on OpenRR-1K [40], revealing fundamental differences in separation strategies.

t-SNE feature distribution. Figure 10 visualizes transmission and reflection features across LFSB decoder levels. DSIT maintains strong separation throughout all levels, which represents an architectural philosophy that prioritizes immediate layer distinction. ReflexSplit demonstrates *progressive disentanglement*: features overlap at Level 4 to facilitate shared feature learning at deep layers, then gradually separate toward Level 0. This curriculum-based strategy $\mathbf{A}^t - \lambda(e)\mathbf{A}^r$ may enable learning shared features before specializing to layer-specific characteristics.

Principal component analysis. Figure 11 shows ReflexSplit features accumulate variance gradually, requiring more principal components to reach 95% threshold—indicating more distributed representations. DSIT exhibits steeper accumulation with variance concentrated in fewer components, suggesting more compact encoding. While both achieve efficient output encoding, ReflexSplit’s intermediate LFSB features require more principal components to capture equivalent variance, which may facilitate progressive layer disentanglement.

These findings validate our differential attention design with curriculum learning, demonstrating that progressive separation represents a viable alternative to immediate separation approaches, particularly for complex real-world reflection removal scenarios.

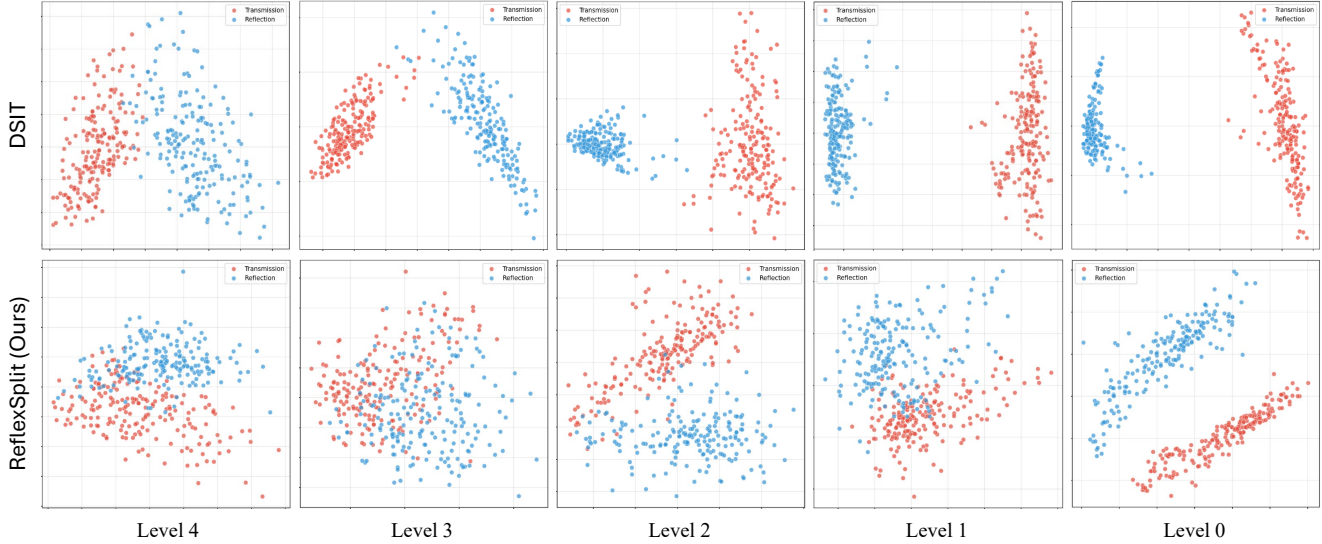


Figure 10. **t-SNE visualization reveals different separation strategies.** DSIT [14] (top) maintains strong separation across all levels, while ReflexSplit (bottom) demonstrates progressive disentanglement from overlap (Level 4) to clear separation (Level 0). Red/blue: transmission/reflection features.

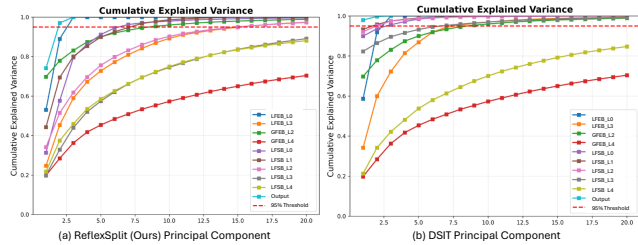


Figure 11. **Cumulative explained variance comparison.** (a) ReflexSplit shows gradual accumulation indicating richer representations. (b) DSIT exhibits steeper accumulation with variance concentrated in fewer components.

9. Comparison with RDNet on Real-World Scenarios

RDNet [43] represents a strong baseline with its reversible architecture that preserves information flow through the network. While implicit feature learning through reversible architectures shows strong performance across diverse scenarios, we observe that explicit layer separation constraints may provide complementary advantages in certain complex cases, particularly scenes with over-exposure, specular highlights, and spatially-varying attenuation.

Table 6 provides a detailed performance margin distribution comparing ReflexSplit and RDNet on OpenRR-1K [40]. ReflexSplit achieves improvements on 63% of test images, with notable gains (>3 dB) on 20% of cases. These improvements are particularly evident in challenging scenarios shown in Figure 12.

We hypothesize that these gains are related to our explicit differential attention mechanism $\mathbf{A}^t - \lambda \mathbf{A}^r$, which provides clear separation constraints at each decoder level. This architectural choice appears to offer advantages for maintaining layer distinction under complex nonlinear mixing, representing a complementary design philosophy to RDNet’s reversible approach. Both strategies demonstrate merit, with performance differences dependent on specific scene characteristics.

10. Additional Visual Comparisons

We provide additional visual comparisons on OpenRR-1K [40] and SIR² [31] datasets in Figures 12–15.

As shown in Figure 12, ReflexSplit achieves cleaner transmission layers in challenging real-world scenarios. Figures 13 and 14 demonstrate consistent performance on synthetic benchmarks across different methods, each exhibiting different characteristics: DSRNet and DSIT show residual reflections in certain regions, MaxRF tends toward aggressive smoothing, while RDNet occasionally exhibits color shifts. Our method aims to balance these trade-offs through explicit layer separation constraints.

11. Failure Cases and Limitations

While ReflexSplit achieves state-of-the-art performance, we observe failure cases in challenging lighting conditions (Figures 16, 17):

Complex outdoor lighting. In outdoor scenes with strong sunlight, shadows, and varying illumination, the nonlinear mixing becomes highly spatially-varying. The separation

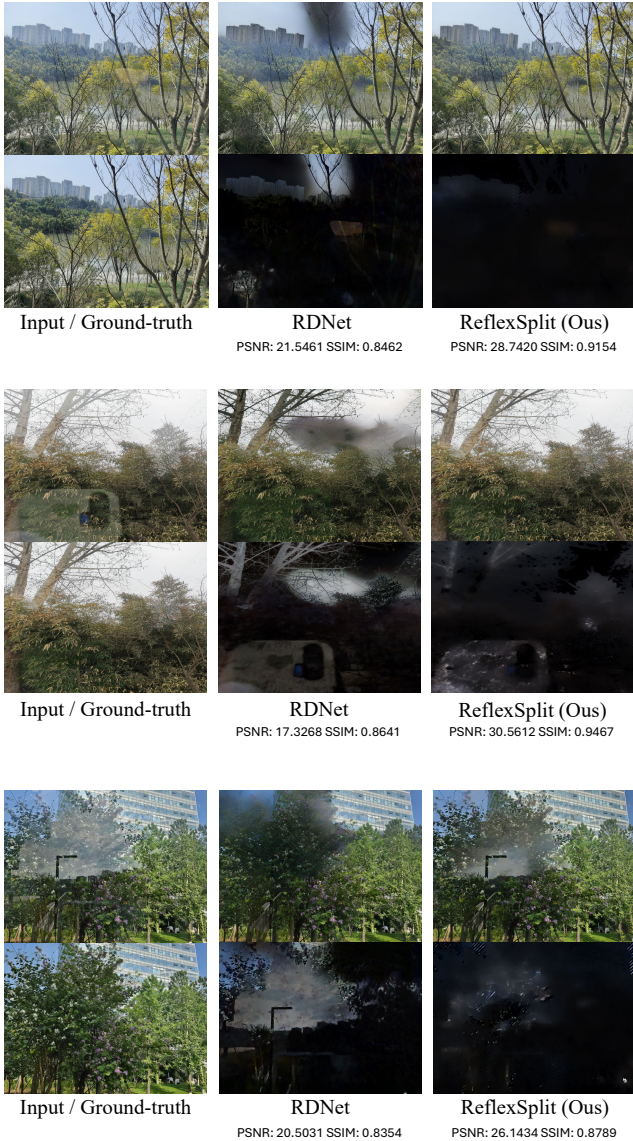


Figure 12. **Challenging real-world scenarios on OpenRR-1K [40]**. Comparison of ReflexSplit with state-of-the-art RDNet [43] on diverse degradation types. Our differential attention mechanism provides explicit layer separation constraints, achieving natural color fidelity and sharp detail preservation in these challenging cases.

becomes particularly challenging when transmission and reflection layers experience different lighting conditions simultaneously, causing inconsistent separation across image regions.

Specular reflections. Strong specular highlights from mirror-like surfaces produce localized over-exposure that saturates both layers. In these regions, the separation becomes ill-posed as no texture information remains to distinguish transmission from reflection—a fundamental chal-

Table 7. Efficiency comparison on 384×384 input resolution.

Method	Params (M)	FLOPs (G)	Time (ms)	FPS	Training Stage	Reflection Separation
DExNet	9.6	995.841	185.114	5.40	Single	✓
MaxRF	27.9	92.135	40.855	24.48	Multiple	×
DSIT	136	867.704	172.199	5.81	Single	✓
RDNet	266.4	1047.141	122.800	8.14	Multiple	✓
DAI	1738.5	7850.567	418.649	2.39	Multiple	×
ReflexSplit	174	969.050	211.349	4.73	Single	✓

lenge for learning-based approaches.

Mixed indoor-outdoor scenes. When capturing indoor scenes through glass with outdoor backgrounds, the extreme brightness difference (often exceeding camera dynamic range) causes either indoor under-exposure or outdoor over-saturation. Reliable layer separation becomes difficult when one component is dominated by noise or clipping artifacts, representing a limitation shared by most decomposition methods.

12. Network Architecture Details

Table 8 details ReflexSplit’s complete architecture across four stages: dual-branch feature extraction (GFEB, LFEB), feature mixing, hierarchical decoding with CrGF and LFSB, and output generation.

13. More Complexity Comparison

Table 7 compares the computational efficiency of ReflexSplit against existing methods on 384×384 input resolution. ReflexSplit achieves a favorable balance between model complexity and task capability. While DAI and RDNet require multiple training stages and incur substantially higher parameter counts (1738.5M and 266.4M, respectively), ReflexSplit completes training in a single stage with 174M parameters, simplifying the training pipeline without sacrificing reflection separation capability. Compared to DExNet and DSIT, which are also single-stage methods supporting reflection separation, ReflexSplit achieves competitive FLOPs (969.050G vs. 995.841G and 867.704G) while offering more comprehensive dual-branch feature modeling. Although MaxRF reports lower FLOPs (92.135G) and faster inference (24.48 FPS), it does not support direct reflection separation, limiting its applicability to this task. Overall, ReflexSplit represents a practical single-stage solution that targets reflection separation with reasonable computational overhead, making it suitable for deployment without the complexity of multi-stage training pipelines.

References

- [1] Amit K Agrawal, Ramesh Raskar, Shree K Nayar, and Yuanzhen Li. Removing photography artifacts using gradient projection and flash-exposure sampling. In *ACM SIG-GRAPH Papers*, pages 828–835, 2005. 2

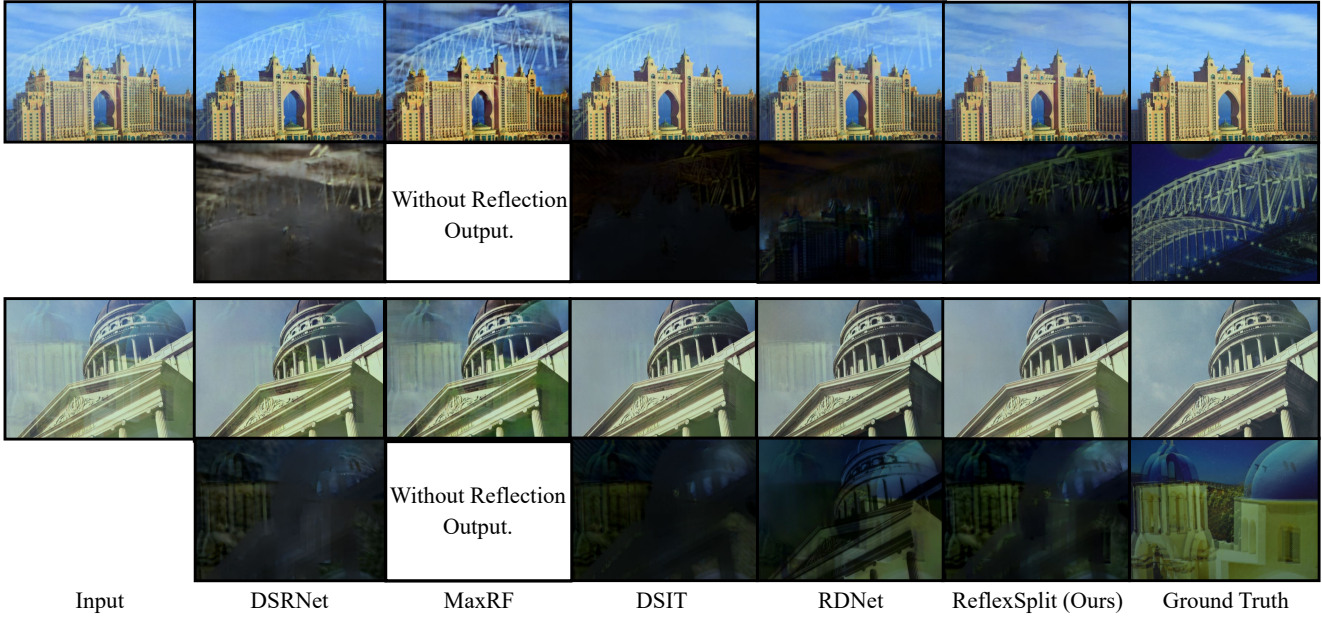


Figure 13. **Qualitative comparison on Postcard [31]**. ReflexSplit achieves superior reflection suppression with faithful detail preservation.

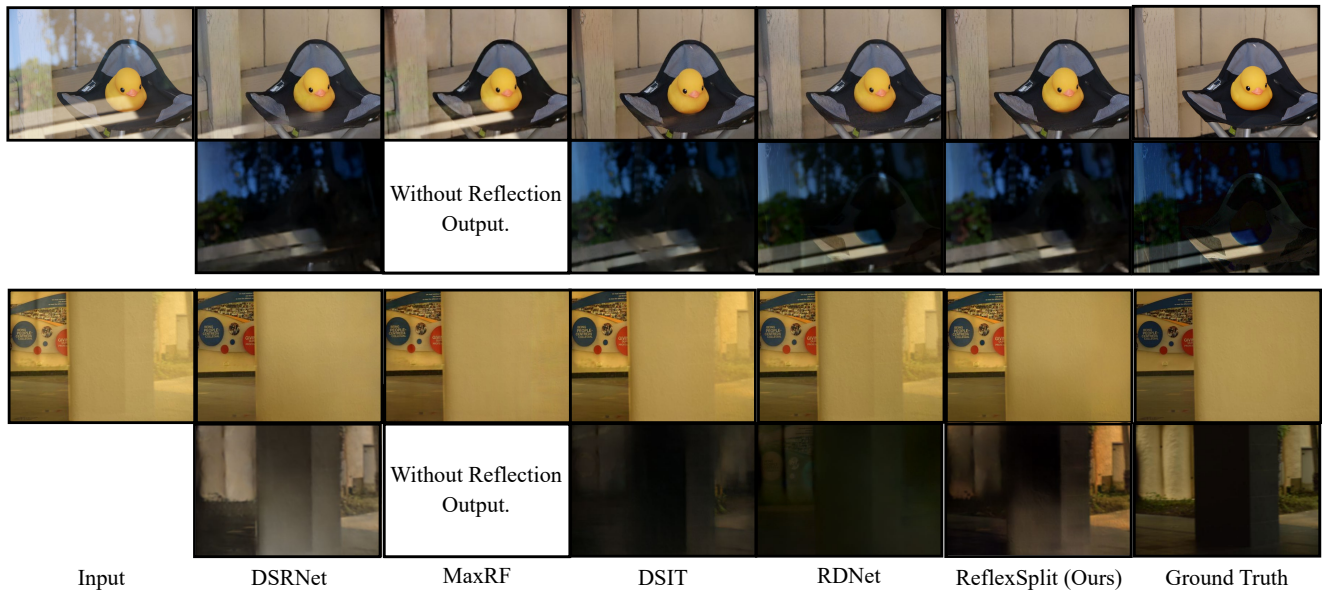


Figure 14. **Qualitative comparison on Wild and SolidObject [31]**.

- [2] Jonathan T. Barron. A general and adaptive robust loss function. In *2019 IEEE/CVF Conference on Computer Vision and Pattern Recognition (CVPR)*, pages 4326–4334, 2019. 5, 2
- [3] Zheng Dong, Ke Xu, Yin Yang, Hujun Bao, Weiwei Xu, and Rynson WH Lau. Location-aware single image reflection removal. In *Proceedings of the IEEE/CVF international conference on computer vision*, pages 5017–5026, 2021. 2
- [4] Mark Everingham, Luc Van Gool, Christopher KI Williams, John Winn, and Andrew Zisserman. The pascal visual object classes (voc) challenge. *International journal of computer vision*, 88:303–338, 2010. 6, 7
- [5] Qingnan Fan, Jiaolong Yang, Gang Hua, Baoquan Chen, and David Wipf. A generic deep architecture for single image reflection removal and image smoothing. In *Proceedings of the IEEE International Conference on Computer Vision*, pages 3238–3247, 2017. 1, 2
- [6] Hany Farid and Edward H Adelson. Separating reflections and lighting using independent components analysis. In *Proceedings of the IEEE Conference on Computer Vision and Pattern Recognition*, pages 1262–1267, 1999. 2
- [7] Xin Feng, Wenjie Pei, Zihui Jia, Fanglin Chen, David Zhang, and Guangming Lu. Deep-masking generative network: A



Figure 15. Additional visualization on OpenRR-1K [40].



Figure 16. Failure cases on OpenRR-1K [40].

unified framework for background restoration from superimposed images. *IEEE Transactions on Image Processing*, 30: 4867–4882, 2021. 2

- [8] Aidan N Gomez, Mengye Ren, Raquel Urtasun, and Roger B Grosse. The reversible residual network: Backpropagation without storing activations. In *Advances in Neural Information Processing Systems*. Curran Associates, Inc., 2017. 1
- [9] Bharath Hariharan, Pablo Arbeláez, Ross Girshick, and Jitendra Malik. Hypercolumns for object segmentation and fine-grained localization. In *2015 IEEE Conference on Computer Vision and Pattern Recognition (CVPR)*, pages 447–456, 2015. 1
- [10] Chih-Chung Hsu, Chia-Ming Lee, and Yi-Shiuan Chou. Drct: Saving image super-resolution away from information bottleneck. In *Proceedings of the IEEE/CVF Conference on Computer Vision and Pattern Recognition (CVPR) Workshops*, pages 6133–6142, 2024. 2
- [11] Jichen Hu, Chen Yang, Zanwei Zhou, Jiemin Fang, Xiaokang Yang, Qi Tian, and Wei Shen. Dereflexion any image with diffusion priors and diversified data, 2025. 3
- [12] Qiming Hu and Xiaojie Guo. Trash or treasure? an interactive dual-stream strategy for single image reflection separation. *Advances in Neural Information Processing Systems*, 34:24683–24694, 2021. 1, 2, 6
- [13] Qiming Hu and Xiaojie Guo. Single image reflection separation via component synergy. In *Proceedings of the IEEE/CVF International Conference on Computer Vision*, pages 13138–13147, 2023. 1, 2, 3, 4, 6, 7
- [14] Qiming Hu, Hainuo Wang, and Xiaojie Guo. Single image reflection separation via dual-stream interactive transformers. *Advances in Neural Information Processing Systems*, 37:55228–55248, 2024. 1, 2, 3, 4, 6, 7
- [15] Jun-Jie Huang, Tianrui Liu, Zihan Chen, Xinwang Liu, Meng Wang, and Pier Luigi Dragotti. A lightweight deep exclusion unfolding network for single image reflection removal. *IEEE Transactions on Pattern Analysis and Machine Intelligence*, 2025. 3, 6



Figure 17. Failure cases on OpenRR-1K [40].

- [16] Naejin Kong, Yu-Wing Tai, and Sung Yong Shin. High-quality reflection separation using polarized images. *IEEE Transactions on Image Processing*, 20(12):3393–3405, 2011. 2
- [17] Yajing Kong, Liu Liu, Jun Wang, and Dacheng Tao. Adaptive curriculum learning. In *2021 IEEE/CVF International Conference on Computer Vision (ICCV)*, pages 5047–5056, 2021. 5
- [18] Chenyang Lei and Qifeng Chen. Robust reflection removal with reflection-free flash-only cues. In *Proceedings of the IEEE/CVF Conference on Computer Vision and Pattern Recognition*, pages 14811–14820, 2021. 2
- [19] Chenyang Lei, Xuhua Huang, Mengdi Zhang, Qiong Yan, Wenxiu Sun, and Qifeng Chen. Polarized reflection removal with perfect alignment in the wild. In *Proceedings of the IEEE/CVF conference on computer vision and pattern recognition*, pages 1750–1758, 2020. 2, 3
- [20] Anat Levin and Yair Weiss. User assisted separation of reflections from a single image using a sparsity prior. *IEEE Transactions on Pattern Analysis and Machine Intelligence*, 29(9):1647–1654, 2007. 2
- [21] Chao Li, Yixiao Yang, Kun He, Stephen Lin, and John E Hopcroft. Single image reflection removal through cascaded refinement. In *Proceedings of the IEEE/CVF conference on computer vision and pattern recognition*, pages 3565–3574, 2020. 3, 6
- [22] Yu Li and Michael S Brown. Single image layer separation using relative smoothness. In *Proceedings of the IEEE conference on computer vision and pattern recognition*, pages 2752–2759, 2014. 2
- [23] Yu Li, Ming Liu, Yaling Yi, Qince Li, Dongwei Ren, and Wangmeng Zuo. Two-stage single image reflection removal with reflection-aware guidance. *Applied Intelligence*, 53(16):19433–19448, 2023. 2
- [24] Yu-Lun Liu, Wei-Sheng Lai, Ming-Hsuan Yang, Yung-Yu Chuang, and Jia-Bin Huang. Learning to see through obstructions. In *Proceedings of the IEEE/CVF Conference on Computer Vision and Pattern Recognition*, pages 14203–14212, 2020. 2
- [25] Ze Liu, Yutong Lin, Yue Cao, Han Hu, Yixuan Wei, Zheng Zhang, Stephen Lin, and Baining Guo. Swin transformer: Hierarchical vision transformer using shifted windows. In *Proceedings of the IEEE/CVF international conference on computer vision*, pages 10012–10022, 2021. 3
- [26] Shree K Nayar, Xi-Sheng Fang, and Terrance Boult. Separation of reflection components using color and polarization. pages 163–186, 1997. 2
- [27] K. Simonyan and A. Zisserman. Very deep convolutional networks for large-scale image recognition. *arXiv preprint arXiv:1409.1556*, 2015. 5, 2
- [28] Sudipta N Sinha, Johannes Kopf, Michael Goesele, Daniel Scharstein, and Richard Szeliski. Image-based rendering for scenes with reflections. *ACM Transactions on Graphics (TOG)*, 31(4):1–10, 2012. 2
- [29] Xuwen Song and Lianpo Wang. Y-ffc net for 3d reconstruction of highly reflective surfaces. *IEEE Transactions on Industrial Informatics*, 20(12):13966–13974, 2024. 1
- [30] Zhenbo Song, Zhenyuan Zhang, Kaihao Zhang, Wenhan Luo, Zhaoxin Fan, Wenqi Ren, and Jianfeng Lu. Robust single image reflection removal against adversarial attacks. In *2023 IEEE/CVF Conference on Computer Vision and Pattern Recognition (CVPR)*, pages 24688–24698, 2023. 3
- [31] Renjie Wan, Boxin Shi, Ling-Yu Duan, Ah-Hwee Tan, and Alex C Kot. Benchmarking single-image reflection removal algorithms. In *Proceedings of the IEEE International Conference on Computer Vision*, pages 3922–3930, 2017. 6, 7, 8, 3, 5
- [32] Renjie Wan, Boxin Shi, Ling-Yu Duan, Ah-Hwee Tan, and Alex C Kot. Crrn: Multi-scale guided concurrent reflection removal network. In *Proceedings of the IEEE Conference on Computer Vision and Pattern Recognition*, pages 4777–4785, 2018. 1, 2
- [33] Renjie Wan, Boxin Shi, Haoliang Li, Ling-Yu Duan, Ah-Hwee Tan, and Alex C Kot. Corrn: Cooperative reflection

Table 8. **Architecture of ReflexSplit**. The model takes a 384×384 input image and processes it through dual-branch encoders (GFEB and LFEB) followed by hierarchical decoding with CrGF and LFSB.

Block Name	Output Size	Transmission Branch	Reflection Branch	Order
<i>Stage 1: Dual-Branch Feature Extraction</i>				
Global Feature Extractor Block (GFEB)				
Swin Transformer Stage 2	$96 \times 96 \times 192$	Shared (\mathbf{P}_2)		1
Swin Transformer Stage 3	$48 \times 48 \times 384$	Shared (\mathbf{P}_3)		2
Swin Transformer Stage 4	$24 \times 24 \times 768$	Shared (\mathbf{P}_4)		3
Swin Transformer Stage 5	$12 \times 12 \times 1536$	Shared (\mathbf{P}_5)		4
Local Feature Extractor Block (LFEB)				
Conv 3x3	$384 \times 384 \times 48$	$3 \rightarrow 48$ (\mathbf{E}_0)	$3 \rightarrow 48$ (\mathbf{E}_0)	1
MuGI Block (x2)	$384 \times 384 \times 48$	$48 \rightarrow 48$	$48 \rightarrow 48$	2
Conv 2x2, stride=2	$192 \times 192 \times 96$	$48 \rightarrow 96$ (\mathbf{E}_1)	$48 \rightarrow 96$ (\mathbf{E}_1)	3
MuGI Block (x2)	$192 \times 192 \times 96$	$96 \rightarrow 96$	$96 \rightarrow 96$	4
Conv 2x2, stride=2	$96 \times 96 \times 192$	$96 \rightarrow 192$ (\mathbf{E}_2)	$96 \rightarrow 192$ (\mathbf{E}_2)	5
MuGI Block (x2)	$96 \times 96 \times 192$	$192 \rightarrow 192$	$192 \rightarrow 192$	6
Conv 2x2, stride=2	$48 \times 48 \times 384$	$192 \rightarrow 384$ (\mathbf{E}_3)	$192 \rightarrow 384$ (\mathbf{E}_3)	7
MuGI Block (x2)	$48 \times 48 \times 384$	$384 \rightarrow 384$	$384 \rightarrow 384$	8
Conv 2x2, stride=2	$24 \times 24 \times 768$	$384 \rightarrow 768$ (\mathbf{E}_4)	$384 \rightarrow 768$ (\mathbf{E}_4)	9
MuGI Block (x2)	$24 \times 24 \times 768$	$768 \rightarrow 768$	$768 \rightarrow 768$	10
Conv 2x2, stride=2	$12 \times 12 \times 1536$	$768 \rightarrow 1536$ (\mathbf{E}_5)	$768 \rightarrow 1536$ (\mathbf{E}_5)	11
<i>Stage 2: Feature Mixing</i>				
Initial Feature Interaction				
PixelShuffle (x2)	$24 \times 24 \times 384$	$1536 \rightarrow 384$	$1536 \rightarrow 384$	5
LFSB (depth=5)	$24 \times 24 \times 384$	$384 \rightarrow 384$	$384 \rightarrow 384$	6
Conv 1x1	$24 \times 24 \times 768$	$384 \rightarrow 768$	$384 \rightarrow 768$	7
LFSB (depth=4)	$24 \times 24 \times 768$	$768 \rightarrow 768$	$768 \rightarrow 768$	8
<i>Stage 3: Hierarchical Decoding with CrGF and LFSB</i>				
Decoder Level 4				
CrGF	$24 \times 24 \times 768$	$\mathbf{P}_4 + \mathbf{E}_4 + \mathbf{F}_5$	$\mathbf{P}_4 + \mathbf{E}_4 + \mathbf{F}_5$	9
LFSB (x12, depth=4)	$24 \times 24 \times 768$	$768 \rightarrow 768$	$768 \rightarrow 768$	10
PixelShuffle (x2)	$48 \times 48 \times 192$	$768 \rightarrow 192$	$768 \rightarrow 192$	11
MuGI Block (x2)	$48 \times 48 \times 192$	$192 \rightarrow 192$	$192 \rightarrow 192$	12
Conv 1x1	$48 \times 48 \times 384$	$192 \rightarrow 384$	$192 \rightarrow 384$	13
Decoder Level 3				
CrGF	$48 \times 48 \times 384$	$\mathbf{P}_3 + \mathbf{E}_3 + \mathbf{F}_4$	$\mathbf{P}_3 + \mathbf{E}_3 + \mathbf{F}_4$	14
LFSB (depth=3)	$48 \times 48 \times 384$	$384 \rightarrow 384$	$384 \rightarrow 384$	15
LFSB (x8, depth=3)	$48 \times 48 \times 384$	$384 \rightarrow 384$	$384 \rightarrow 384$	16
PixelShuffle (x2)	$96 \times 96 \times 96$	$384 \rightarrow 96$	$384 \rightarrow 96$	17
MuGI Block (x2)	$96 \times 96 \times 96$	$96 \rightarrow 96$	$96 \rightarrow 96$	18
Conv 1x1	$96 \times 96 \times 192$	$96 \rightarrow 192$	$96 \rightarrow 192$	19
Decoder Level 2				
CrGF	$96 \times 96 \times 192$	$\mathbf{P}_2 + \mathbf{E}_2 + \mathbf{F}_3$	$\mathbf{P}_2 + \mathbf{E}_2 + \mathbf{F}_3$	20
LFSB (depth=2)	$96 \times 96 \times 192$	$192 \rightarrow 192$	$192 \rightarrow 192$	21
LFSB (x4, depth=2)	$96 \times 96 \times 192$	$192 \rightarrow 192$	$192 \rightarrow 192$	22
PixelShuffle (x2)	$192 \times 192 \times 48$	$192 \rightarrow 48$	$192 \rightarrow 48$	23
MuGI Block (x2)	$192 \times 192 \times 48$	$48 \rightarrow 48$	$48 \rightarrow 48$	24
Conv 1x1	$192 \times 192 \times 96$	$48 \rightarrow 96$	$48 \rightarrow 96$	25
Decoder Level 1				
Direct Aggregation	$192 \times 192 \times 96$	$\mathbf{E}_1 + \mathbf{F}_2$	$\mathbf{E}_1 + \mathbf{F}_2$	26
LFSB (x2, depth=1)	$192 \times 192 \times 96$	$96 \rightarrow 96$	$96 \rightarrow 96$	27
PixelShuffle (x2)	$384 \times 384 \times 24$	$96 \rightarrow 24$	$96 \rightarrow 24$	28
MuGI Block (x2)	$384 \times 384 \times 24$	$24 \rightarrow 24$	$24 \rightarrow 24$	29
Conv 1x1	$384 \times 384 \times 48$	$24 \rightarrow 48$	$24 \rightarrow 48$	30
Decoder Level 0				
Direct Aggregation	$384 \times 384 \times 48$	$\mathbf{E}_0 + \mathbf{F}_1$	$\mathbf{E}_0 + \mathbf{F}_1$	31
LFSB (x2, depth=0)	$384 \times 384 \times 48$	$48 \rightarrow 48$	$48 \rightarrow 48$	32
MuGI Block (x2)	$384 \times 384 \times 48$	$48 \rightarrow 48$	$48 \rightarrow 48$	33
<i>Stage 4: Output Generation</i>				
Conv 3x3	$384 \times 384 \times 3$	$48 \rightarrow 3$ ($\hat{\mathbf{T}}$)	$48 \rightarrow 3$ ($\hat{\mathbf{R}}$)	34
Learnable Residue Module (LRM)				
Feature Aggregation	$384 \times 384 \times 48$	$\mathbf{F}_0^l + \mathbf{F}_0^r$		35
SinBlock	$384 \times 384 \times 48$	$48 \rightarrow 48$		36
Conv 3x3 + Tanh	$384 \times 384 \times 3$	$48 \rightarrow 3$ ($\hat{\mathbf{R}}\hat{\mathbf{R}}$)		37

- removal network. *IEEE transactions on pattern analysis and machine intelligence*, 42(12):2969–2982, 2019. 2
- [34] Renjie Wan, Boxin Shi, Haoliang Li, Ling-Yu Duan, and Alex C Kot. Reflection scene separation from a single image. In *Proceedings of the IEEE/CVF Conference on Computer Vision and Pattern Recognition*, pages 2398–2406, 2020. 2
- [35] Linhan Wang, Kai Cheng, Shuo Lei, Shengkun Wang, Wei Yin, Chenyang Lei, Xiaoxiao Long, and Chang-Tien Lu. Dc-gaussian: Improving 3d gaussian splatting for reflective dash cam videos. *Advances in Neural Information Processing Systems*, 37:99898–99920, 2024. 1
- [36] Kaixuan Wei, Jiaolong Yang, Ying Fu, David Wipf, and Hua Huang. Single image reflection removal exploiting misaligned training data and network enhancements. In *Proceedings of the IEEE/CVF Conference on Computer Vision and Pattern Recognition*, pages 8178–8187, 2019. 6
- [37] Qiang Wen, Yinjie Tan, Jing Qin, Wenxi Liu, Guoqiang Han, and Shengfeng He. Single image reflection removal beyond linearity. In *Proceedings of the IEEE/CVF Conference on Computer Vision and Pattern Recognition*, pages 3771–3779, 2019. 2
- [38] Tianfan Xue, Michael Rubinstein, Ce Liu, and William T Freeman. A computational approach for obstruction-free photography. *ACM Transactions on Graphics (TOG)*, 34(4): 1–11, 2015. 2
- [39] Jie Yang, Dong Gong, Lingqiao Liu, and Qinfeng Shi. Seeing deeply and bidirectionally: A deep learning approach for single image reflection removal. In *Proceedings of the european conference on computer vision (ECCV)*, pages 654–669, 2018. 2
- [40] Kangning Yang, Ling Ouyang, Huiming Sun, Jie Cai, Lan Fu, Jiaming Ding, Chiu Man Ho, and Zibo Meng. Openrr-1k: A scalable dataset for real-world reflection removal, 2025. 1, 6, 2, 3, 4, 7
- [41] Tianzhu Ye, Li Dong, Yuqing Xia, Yutao Sun, Yi Zhu, Gao Huang, and Furu Wei. Differential transformer. In *The Thirteenth International Conference on Learning Representations*, 2025. 4
- [42] Xuaner Zhang, Ren Ng, and Qifeng Chen. Single image reflection separation with perceptual losses. In *Proceedings of the IEEE conference on computer vision and pattern recognition*, pages 4786–4794, 2018. 1, 6, 2
- [43] Hao Zhao, Mingjia Li, Qiming Hu, and Xiaojie Guo. Reversible decoupling network for single image reflection removal. *arXiv preprint arXiv:2410.08063*, 2024. 1, 2, 3, 4, 6, 7
- [44] Qian Zheng, Boxin Shi, Jinnan Chen, Xudong Jiang, Ling-Yu Duan, and Alex C Kot. Single image reflection removal with absorption effect. In *Proceedings of the IEEE/CVF Conference on Computer Vision and Pattern Recognition*, pages 13395–13404, 2021. 2, 6
- [45] Haofeng Zhong, Yuchen Hong, Shuchen Weng, Jinxiu Liang, and Boxin Shi. Language-guided image reflection separation. In *Proceedings of the IEEE/CVF Conference on Computer Vision and Pattern Recognition*, pages 24913–24922, 2024. 3, 6
- [46] Yurui Zhu, Xueyang Fu, Zheyu Zhang, Aiping Liu, Zhiwei Xiong, and Zheng-Jun Zha. Hue guidance network for single image reflection removal. *IEEE transactions on neural networks and learning systems*, 2023. 3
- [47] Yurui Zhu, Xueyang Fu, Peng-Tao Jiang, Hao Zhang, Qibin Sun, Jinwei Chen, Zheng-Jun Zha, and Bo Li. Revisiting single image reflection removal in the wild. In *Proceedings of the IEEE/CVF Conference on Computer Vision and Pattern Recognition*, pages 25468–25478, 2024. 6, 7